Scattering theory of subsurface impurities observed in scanning tunneling microscopy

Katsuyoshi Kobayashi
Department of Physics, Faculty of Science, Ochanomizu University, 2-1-1 Otsuka, Bunkyo-ku, Tokyo 112, Japan
(Received 4 June 1996; revised manuscript received 23 July 1996)

Subsurface impurities observed in scanning tunneling microscopy (STM) are investigated theoretically. As a scattering potential of the impurities, the screened Coulomb potential is used. Wave functions are solved exactly by numerical calculations. Qualitative behavior of STM images is discussed in terms of analytical expressions derived perturbatively, and the origin of the Friedel oscillation observed in STM images of subsurface impurities is clarified. It is found that to produce the Friedel oscillation, the spatial range of the impurity potential must be shorter than the Fermi wavelength. In the short-range case, calculated STM images show oscillating behavior also as a function of the depth of impurities. When the depth is small, the corrugation amplitude increases with the increase of the depth and reaches the maximum at the depth of about the Fermi wavelength. Ring structures observed in STM of transition-metal-dichalcogenide surfaces are also explained by the subsurface impurities. [S0163-1829(96)07648-5]

I. INTRODUCTION

Recently, bulk defects in semiconductor surfaces have been studied extensively by scanning tunneling microscopy (STM). Donor states have been detected in scanning tunneling spectroscopy (STS) of the GaAs surface.[1] Images of subsurface impurities have been observed clearly in STM, even when they are buried by several layers underneath the surfaces. [2–5] Charge states of bulk defects have been discussed by studying the interaction between defects.[6–8] Moreover, the Friedel oscillation around the images of the subsurface impurities has been observed by low-temperature STM.[9] These observations of subsurface defects by STM are not trivial, because STM images reflect electronic structures of surfaces in the vacuum region where the influence of the outermost layers is dominant. Subsurface structures are usually not observed in STM.

A mechanism explaining the observations of subsurface structures in STM has been proposed recently,[10] where it has been concluded that subsurface structures are visible if they have a nanometer-scale lateral dimension, but atomic-scale structures are not visible. The key point of this result is that nanoscale waves propagate in materials without decay, but atomic-scale waves decay rapidly in the atomic scale.

From this point of view, the observations of subsurface impurities may not be curious. Indeed, the subsurface impurities themselves are atomic-scale structures, but if there is any cause producing nanometer-scale waves, they are visible. In the case of the donor impurity in the GaAs(110) surface, a naive interpretation of the STM images may be that the donor level is observed, because the orbitals of bulk donor levels in semiconductors extend over several nanometers. However, this naive interpretation is questionable, because the donor levels near surfaces are different from those in the bulk.

Properties of the donor levels near surfaces have been studied by several authors.[11–14] In an extreme case of a donor lying just on a surface and an infinite work function, the s state is not allowed.[11] The possible state with the lowest energy is the p_z state where z is perpendicular to the surface. The wave function of the p_z state is zero at the surface $z=0$, the donor states are not visible in this case. Since real impurities do not lie just on surfaces and work functions are finite, this extreme case is oversimplified. But, it is questionable to interpret the STM images simply in terms of the conventional donor states in the bulk.

Moreover, it is not possible to explain the Friedel oscillation by the bulk donor states, because the $1s$ state does not show the oscillating behavior. Since subsurface impurities are observed at bias voltages corresponding to the energy regions outside the band gap, it would be better to interpret the STM images in terms of the scattering of electrons in bulk bands by the subsurface impurities.

In this paper, we study theoretically STM images of subsurface impurities, in order to clarify the mechanism of observing the Friedel oscillation by STM. Scattering properties by subsurface impurities are investigated using the screened Coulomb potential. It is found that to observe the Friedel oscillation, the range of the scattering potential is much shorter than Fermi wavelengths. In this short-range case, the corrugation amplitude of the subsurface impurities increases with the increase of the depth and reaches the maximum at the depth of about the Fermi wavelength, in contrast to the intuitive picture.

In Sec. II, we discuss scattering properties by the screened Coulomb potential. To understand qualitative properties, we present some analytical expressions derived perturbatively and clarify how it occurs that the Friedel oscillation is observed in the STM images. To verify the results obtained by the perturbative treatment, we perform numerical calculations and solve exactly the scattering problem by the screened Coulomb potential near surfaces in Sec. III. In Sec. IV, we compare theoretical results with experimental observations and speculate the depth and screening length of subsurface impurities. Nanometer-scale structures observed on other surfaces are discussed in terms of the subsurface impurities. In this paper, we use the atomic units ($\hbar=m=e=1$), if units are not shown explicitly.

II. SCATTERING PROPERTIES BY THE SCREENED COULOMB POTENTIAL

In discussing the shallow impurity levels in semiconductors, we usually use the effective potential

$$V_{\rm eff}(r) = -\frac{1}{\epsilon r}, \tag{2.1}$$

where ϵ is the dielectric constant. A solution of the Schrödinger equation with this potential is the $1s$ orbital such as the hydrogen atom. Since the radius of the impurity orbital is typically 100 times larger than the Bohr radius, there is an interpretation that the bright spots observed in STM images are the impurity orbital. However, this naive interpretation is not right, because the Friedel oscillation observed around the bright spots cannot be explained by the nodeless $1s$ orbital. In addition, the impurity level is a localized orbital, which carries no current and, therefore, should not be observed in STM without taking account of the band bending. The images of the subsurface impurities are observed when the bias voltage corresponds to the energy regions outside the band gap. Therefore, it would be more reasonable to interpret the bright spots observed in STM as the images of conduction or valence electrons scattered by the impurity potential. In this paper, we investigate the scattering behavior of electrons in bulk bands.

The effective potential for the band electrons is different from that shown in Eq. (2.1), because the screening effect by the electron in the impurity level is not taken into account in $V_{\rm eff}$. In this paper, we adopt the screened Coulomb potential given by

$$V(r) = f_0 \frac{e^{-\mu r}}{r}, \tag{2.2}$$

as the effective potential. In the above, f_0 and μ are the strength of the scattering potential and the inverse of the screening length, respectively. In this section, we solve perturbatively wave functions of electrons scattered by this effective potential located near surfaces.

The two-dimensional Fourier transformation of the screened Coulomb potential is given by

$$V(z,\mathbf{q}) = \frac{f_0}{2\pi} \frac{e^{-\mu_q |z|}}{\mu_q}, \tag{2.3}$$

where $\mathbf{q}=(q_x,q_y)$ and $\mu_q = \sqrt{\mu^2+q^2}$. When wave functions are expanded in terms of lateral momentum $\mathbf{q}$ as

$$\Psi(\mathbf{r}) = \int A(\mathbf{q},z) e^{i\mathbf{q}\cdot\mathbf{r}_\parallel} d^2q, \tag{2.4}$$

the function $A(\mathbf{q},z)$ satisfies an equation of

$$-\frac{1}{2}\frac{d^2}{dz^2}A(\mathbf{q},z) + \int V(z,\mathbf{q}-\mathbf{q}')A(\mathbf{q}',z)d^2q' = \left(E-\frac{q^2}{2}\right)A(\mathbf{q},z). \tag{2.5}$$

This equation can be solved as

$$A(\mathbf{q},z) = A^0(\mathbf{q},z) + \int G(\mathbf{q},z-z') \times \left[\int V(z',\mathbf{q}-\mathbf{q}')A(\mathbf{q}',z')d^2q'\right]dz', \tag{2.6}$$

by using the Green's function $G(\mathbf{q},z)$ defined as

$$\left(E-\frac{q^2}{2}+\frac{1}{2}\frac{d^2}{dz^2}\right)G(\mathbf{q},z) = \delta(z). \tag{2.7}$$

$A^0(\mathbf{q},z)$ is the unperturbed solution without the scattering potential.

The solution of the Green's function is given by

$$G(\mathbf{q},z) = \frac{e^{ik_z^q|z|}}{ik_z^q}, \tag{2.8}$$

where

$$k_z^q = \begin{cases} \sqrt{k^2-q^2} & (q<k) \\ i\sqrt{q^2-k^2} & (q>k), \end{cases} \tag{2.9}$$

and $k^2/2=E$.

As the unperturbed wave function, we choose a plane wave with lateral momentum $\mathbf{q}_0$ as

$$A^0(\mathbf{q},z) = e^{ik_z^0 z}\delta(\mathbf{q}-\mathbf{q}_0), \tag{2.10}$$

where $k_z^0 = \sqrt{k^2-q_0^2}$. When we remain up to the first-order term in the scattering potential (the Born approximation), we obtain

$$A(\mathbf{q},z) = e^{ik_z^0 z}\delta(\mathbf{q}-\mathbf{q}_0) + \frac{f_0}{\pi i}\frac{e^{ik_z^q z}}{k_z^q}\frac{1}{\mu_q^2+(k_z^q-k_z^0)^2} \quad (z>0). \tag{2.11}$$

In the above, we neglect the terms exponentially decaying as $e^{-\mu_q z}$, because we are interested in the behavior of wave functions at the region outside the potential range of $1/\mu$.

We hitherto have not taken account of the presence of surfaces. If surfaces are present, we must take account of the waves scattered at the surfaces, and Eq. (2.11) is changed into

$$A(\mathbf{q},z) = (e^{ik_z^0 z} + R_0' e^{-ik_z^0 z})\delta(\mathbf{q}-\mathbf{q}_0) + \frac{f_0}{\pi i}\frac{e^{ik_z^q z}+R_q' e^{-ik_z^q z}}{k_z^q}\left[\frac{1}{\mu_q^2+(k_z^q-k_z^0)^2} + R_0'\frac{1}{\mu_q^2+(k_z^q+k_z^0)^2}\right] \quad (0<z<d), \tag{2.12}$$

where R_0' and R_q' are the reflection coefficients with phase factors determined as follows. We assume that the subsurface impurity is buried at a depth d from the surface. When we change the origin of the z axis from the center of the scattering potential to the surface by replacing z by $z+d$ and multiply a phase factor $e^{-ik_z^0 d}$, Eq. (2.12) is modified as

$$A(\mathbf{q},z)=(e^{ik_z^0 z}+R_0e^{-ik_z^0 z})\,\delta(\mathbf{q}-\mathbf{q}_0)+\frac{f_0}{\pi i}\,\frac{e^{ik_z^q z}+R_q e^{-ik_z^q z}}{k_z^q}\,e^{i(k_z^q-k_z^0)d}\left[\frac{1}{\mu_q^2+(k_z^q-k_z^0)^2}+R_0'\frac{1}{\mu_q^2+(k_z^q+k_z^0)^2}\right]\quad(-d<z<0),\tag{2.13}$$

where $R_0=R_0'e^{-2ik_z^0 d}$ and $R_q=R_q'e^{-2ik_z^q d}$ are the reflection coefficients given by

$$R_0=-\frac{\lambda_0+ik_z^0}{\lambda_0-ik_z^0},\tag{2.14}$$

and

$$R_q=-\frac{\lambda_q+ik_z^q}{\lambda_q-ik_z^q}.\tag{2.15}$$

In the above, λ_0 and λ_q are the decay constants in the vacuum region given, respectively, as $\lambda_0=\sqrt{2W+q_0^2}$ and $\lambda_q=\sqrt{2W+q^2}$, where W is the work function.

The wave functions in the vacuum region are obtained by replacing $e^{ik_z^0 z}+R_0e^{-ik_z^0 z}$ and $e^{ik_z^q z}+R_qe^{-ik_z^q z}$, respectively, by $T_0e^{-\lambda_0 z}$ and $T_qe^{-\lambda_q z}$, where $T_0=2ik_z^0/(ik_z^0-\lambda_0)$ and $T_q=2ik_z^q/(ik_z^q-\lambda_q)$. Finally, we obtain an expression for the wave function as

$$\Psi(\mathbf{r};\mathbf{q}_0,d)=T_0e^{i\mathbf{q}_0\cdot\mathbf{r}_\parallel}e^{-\lambda_0 z}+\frac{f_0}{\pi i}\int F(\mathbf{q};\mathbf{q}_0,d)e^{-\lambda_q z}e^{i\mathbf{q}\cdot\mathbf{r}_\parallel}d^2q\quad(z>0),\tag{2.16}$$

where

$$F(\mathbf{q};\mathbf{q}_0,d)\equiv\left(\frac{T_q}{k_z^q}\right)\left[\frac{e^{i(k_z^q-k_z^0)d}}{\mu_q^2+(k_z^q-k_z^0)^2}+R_0\frac{e^{i(k_z^q+k_z^0)d}}{\mu_q^2+(k_z^q+k_z^0)^2}\right].\tag{2.17}$$

The first term of $F(\mathbf{q};\mathbf{q}_0,d)$ originates from the forward scattering of the incident wave by the impurity, whereas the second term comes from the backward scattering of the reflective wave produced from the incident wave at the surface. Note that when $q>k$, k_z^q is pure imaginary and the component decays with the depth d of the impurity. The component with $q<k$ is a propagating wave and does not decay with the depth. Therefore, we expect that at large depths, we cannot observe structures smaller than $1/k_F$.

By performing a hemispherical integral over the equienergy surface, we obtain the local density of states (LDOS) per spin as

$$\rho(\mathbf{r},E)=\frac{k}{(2\pi)^3}\int_{k_z>0}|\Psi|^2d\Omega,\tag{2.18}$$

where Ω is the solid angle. If we assume that the orbital of the tip apex is the s wave, the tunneling current can be approximated by the LDOS with $E=E_F$ at a low bias voltage.[15] Though the LDOS is not accurate enough to reproduce quantitatively corrugation amplitudes of many STM images, it is sufficient to discuss qualitatively the contrast of STM images. For a finite bias voltage V, STM images are obtained by integrating the LDOS over the energy region from E_F to E_F+eV.

Before presenting numerical results, we consider some limiting cases. We assume $k_F\ll\sqrt{2W}$. This condition is satisfied in the case of semiconductors at a low bias voltage. Therefore, we obtain $T_0\simeq-2ik_z^0/\sqrt{2W}$, $T_q\simeq-2ik_z^q/\sqrt{2W}$, $R_0\simeq-1$, and $\lambda_0\simeq\lambda_q\simeq\sqrt{2W}$. Then, the wave function is approximated as

$$\Psi(\mathbf{r};\mathbf{q}_0,d)\simeq-\frac{2i}{\sqrt{2W}}e^{-\sqrt{2W}z}\left\{k_z^0e^{i\mathbf{q}_0\cdot\mathbf{r}_\parallel}+\frac{f_0}{\pi i}\int\left[\frac{e^{i(k_z^q-k_z^0)d}}{\mu_q^2+(k_z^q-k_z^0)^2}-\frac{e^{i(k_z^q+k_z^0)d}}{\mu_q^2+(k_z^q+k_z^0)^2}\right]\times e^{i\mathbf{q}\cdot\mathbf{r}_\parallel}d^2q\right\}.\tag{2.19}$$

Since the wave function is decoupled as a function of $\mathbf{r}_\parallel$ and z, the corrugation amplitude does not depend on the tip-surface distance. This is a common feature of STM images with nanoscale lateral dimensions.[10]

In the present paper, STM images are discussed in terms of the LDOS. This implies that the orbital of the tip apex is assumed to be the s wave.[15] When the tip orbital is the d wave, atomic-scale corrugation amplitudes are much enhanced, which is an important effect in explaining the corrugation amplitudes of metals.[16] However, in the case of waves with nanoscale lateral dimensions, the enhancement factor by the d wave is almost unity because of $k_F\ll\sqrt{2W}$. Therefore, the results obtained in this paper are generally true irrespective of the types of the tip orbitals. This is also a feature characteristic of the nanoscale waves.[10]

A. Case of $\mu\gg k_F$

First, we consider the case $\mu\gg k_F$. In this case, the integrand in Eq. (2.19) is approximated as $-(2i/\mu^2)e^{ik_z^q d}\sin(k_z^0 d)e^{i\mathbf{q}\cdot\mathbf{r}_\parallel}$ and the integrals with $\mathbf{q}_0$ and $\mathbf{q}$ are decoupled. This means physically that the scattering potential is so localized that the scattered wave propagates like the s wave.

The LDOS at the Fermi energy is calculated as

$$\rho(\mathbf{r},E_F)=\frac{1}{(2\pi)^3W}\,\frac{4\pi k_F^3}{3}e^{-2\sqrt{2W}z}\times\left[1-\frac{24f_0k_F}{\mu^2}P(k_Fr_\parallel,k_Fd)Q(k_Fr_\parallel,k_Fd)\right],\tag{2.20}$$

where

$$P(x,y)=\int_0^{\pi/2}J_0(x\sin\theta)\sin(y\cos\theta)\cos\theta\sin\theta\,d\theta,\tag{2.21}$$

and

$$Q(x,y)=\int_0^{\pi/2} J_0(x\sin\theta)\cos(y\cos\theta)\cos\theta\sin\theta d\theta, \qquad (2.22)$$

and $J_0(x)$ is the Bessel function. In the above, the part $q>k_F$ of the integral in Eq. (2.19) and the second-order term in the scattering strength f_0 are neglected. Using the identity,

$$\int_0^{\pi/2} J_0(x\sin\theta)\cos(y\cos\theta)\sin\theta d\theta=\frac{\sin u}{u}, \qquad (2.23)$$

where $u\equiv\sqrt{x^2+y^2}$, we obtain

$$P(x,y)=-\frac{y}{u^2}\left(\cos u-\frac{\sin u}{u}\right). \qquad (2.24)$$

$Q(x,y)$ is not expressed in terms of elementary functions, but it may be approximated by

$$\begin{aligned} Q'(x,y)&\equiv\int_0^{\pi/2} J_0(x\sin\theta)\cos(y\cos\theta)\cos^2\theta\sin\theta d\theta \\ &=\frac{\partial P(x,y)}{\partial y} \\ &=\frac{y^2}{u^3}\sin u-\frac{u^2-3y^2}{u^4}\left(\cos u-\frac{\sin u}{u}\right). \end{aligned} \qquad (2.25)$$

More simply, $Q(x,y)$ is approximated by $\sin(u)/u$ when $x\sim y\gg 1$. In this case, the corrugation $\Delta z(r_\parallel,d)\equiv z(r_\parallel,d)-z(\infty,d)$ is given by

$$\Delta z(r_\parallel,d)=\frac{1}{2\sqrt{2W}}\ln\left[1+\frac{24f_0k_F}{\mu^2}\times\frac{k_Fd}{(k_F\sqrt{r_\parallel^2+d^2})^3}\frac{\sin(2k_F\sqrt{r_\parallel^2+d^2})}{2}\right]. \qquad (2.26)$$

This means that STM images show the Friedel oscillation with the period of $1/(2k_F)$ only at large $r_\parallel\gg d$. It should be noted that when the impurities are buried deep in the subsurface, the period of the oscillation observed in STM images is much larger than $1/(2k_F)$.

When $r_\parallel\ll d$, STM images show the Friedel oscillation with the depth d at fixed $r_\parallel$. Especially, since $Q(0,y)$ is easily calculated, the corrugation at $r_\parallel=0$ is given by

$$\Delta z(0,d)=\frac{1}{2\sqrt{2W}}\ln\left[1+\frac{24f_0k_F}{\mu^2}\frac{1}{(k_Fd)^2}\left(\sin(k_Fd)+\frac{\cos(k_Fd)-1}{k_Fd}\right)\left(\cos(k_Fd)-\frac{\sin(k_Fd)}{k_Fd}\right)\right]. \qquad (2.27)$$

This means that STM images of an impurity show both the positive and negative corrugations, and the polarity of the impurity charge is not determined simply from the sign of the corrugation.

When the depth d is much smaller than $1/k_F$, the corrugation is approximated as

$$\Delta z(0,d)\sim\frac{1}{2\sqrt{2W}}\ln\left[1-\frac{2f_0k_F}{\mu^2}(k_Fd)\right]. \qquad (2.28)$$

This means that impurities charged positively and negatively show positive and negative corrugations at small depths, respectively. It should be noted that the corrugation amplitude increases with the increase of the depth d and reaches the maximum value at about the depth with $2k_Fd\sim\pi/2$. In other words, there is a depth where images of subsurface impurities are most clearly observed. This result is in striking contrast to the intuitive picture that the corrugation of subsurface impurities decreases monotonously with the increase of the depth. This is due to the fact that the nanoscale lateral waves are propagating ones. Standing waves are formed near the surface, and the surface plane is a node of the waves. Therefore, the corrugation decreases as the impurity approaches the surface plane. In contrast with the nanoscale corrugations, atomic corrugations decay exponentially as the depth of impurities increases.

B. Case of $\mu\ll k_F$

Next, we consider the case $\mu\ll k_F$. In this case, the part contributing most to the integral in Eq. (2.19) is the first term of the integrand around the region of $|\mathbf{q}-\mathbf{q}_0|\leqslant\mu$. The second term can be neglected. This corresponds to the fact that the forward scattering is very strong in the Coulomb scattering. The second term produced by the reflection at the surface forms the standing wave by the interference with the first term in the case $\mu\gg k_F$. In the case $\mu\ll k_F$, the second term is neglected, and the scattering behavior resembles the bulk one without the surface. Therefore, we estimate the LDOS in terms of the bulk scattering theory.

In the standard scattering theory, the wave function is written as

$$\Psi(\mathbf{r})=e^{i\mathbf{k}\cdot\mathbf{r}}+f(\theta)\frac{e^{ikr}}{r}, \qquad (2.29)$$

where $f(\theta)$ is the scattering amplitude. In the case of the screened Coulomb potential, it is given in the Born approximation as

$$f(\theta)=-2f_0\frac{1}{\mu^2+q^2}, \qquad (2.30)$$

where $q=2k\sin(\theta/2)$.

By integrating the absolute square of the wave function with respect to the angle of the incident waves, the LDOS is calculated as

$$\rho(\mathbf{r},E)=\frac{k}{(2\pi)^2}\int_0^1\left\{1-\frac{4f_0}{r}\frac{\cos[kr(1-\cos\theta)]}{\mu^2+q^2}+\frac{4f_0^2}{r^2}\frac{1}{(\mu^2+q^2)^2}\right\}d(\cos\theta)$$
$$=\frac{k}{(2\pi)^2}\left[1-\frac{2f_0}{k^2r}H\left(\frac{\mu^2 r}{2k}\right)+\frac{2f_0^2}{\mu^2k^2r^2}+O\left(\left(\frac{\mu}{k}\right)^2\right)\right], \quad (2.31)$$

where

$$H(x)\equiv\int_0^\infty\frac{\cos(xt)}{1+t}dt=\int_0^\infty\frac{te^{-xt}}{1+t^2}dt=-[\sin(x)\mathrm{si}(x)+\cos(x)\mathrm{ci}(x)]. \quad (2.32)$$

In the above, $\mathrm{si}(x)$ and $\mathrm{ci}(x)$ are the integrated sine and cosine functions defined as

$$\mathrm{si}(x)=-\int_x^\infty\frac{\sin t}{t}dt,$$
$$\mathrm{ci}(x)=-\int_x^\infty\frac{\cos t}{t}dt. \quad (2.33)$$

They behave as

$$\mathrm{si}(x)\sim-\frac{\cos x}{x}-\frac{\sin x}{x^2},$$
$$\mathrm{ci}(x)\sim\frac{\sin x}{x}-\frac{\cos x}{x^2}, \quad (2.34)$$

in the limit of $x\to\infty$ and

$$\mathrm{si}(x)\sim-\frac{\pi}{2},$$
$$\mathrm{ci}(x)\sim\ln x, \quad (2.35)$$

in the limit of $x\to0$. Therefore, $H(x)$ behaves as

$$H(x)\sim\frac{1}{x^2}\quad(x\to\infty), \quad (2.36)$$

and

$$H(x)\sim\ln\left(\frac{1}{x}\right)\quad(x\to0). \quad (2.37)$$

In discussing STM images, r in Eq. (2.31) is read as $r=\sqrt{r_\parallel^2+d^2}$. Since $H(x)$ is a monotonously deceasing function with increasing x, STM images do not show the Friedel oscillation in the case of $\mu\ll k$. The corrugation at a large distance is given as

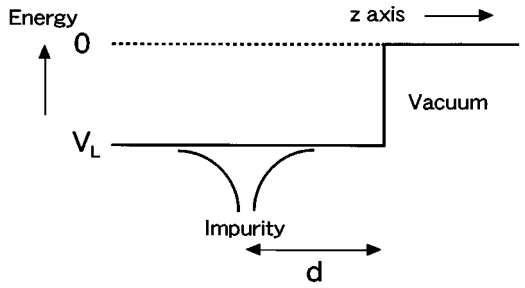

FIG. 1. Schematic of the model potential used in the numerical calculations.

$$\Delta z(r,d)=\frac{1}{2\sqrt{2W}}\ln\left[1-\frac{8f_0}{\mu^4(\sqrt{r_\parallel^2+d^2})^3}+\frac{2f_0^2}{\mu^2k^2(r_\parallel^2+d^2)}\right]. \quad (2.38)$$

The first-order term in the scattering strength f_0 decreases more rapidly than the second-order term at a large distance, and the former is neglected in the standard theory of the bulk scattering. In STM images as shown in the next section, we are interested in the region of $k_Fr\leqslant(k_F/\mu)^2(k_F/f_0)$, and the second-order term is neglected. Therefore, the corrugation decreases monotonously as $\sim1/r^3$ as a function of both $r_\parallel$ and d. This is quite a contrast to the case of $\mu\gg k$. This means that in the condition where the Friedel oscillation is observed as Ref. 9, the scattering potential is well localized and the scattered waves are spherically symmetric.

In the above, we estimate the LDOS in the vacuum region by that in the bulk. The difference between the two LDOS is the coefficients T_0 and T_q in the wave functions of the vacuum region as shown in Eq. (2.16). Since these coefficients are approximately proportional to k_z, the weight of k_z is added in evaluating the LDOS in the vacuum region. This results in a reduction of the corrugation amplitude, but qualitative features are not much changed. Therefore, it is valid to discuss STM images by the LDOS in the bulk.

III. NUMERICAL CALCULATIONS

In this section, we present numerical results of the scattering by subsurface impurities. Figure 1 shows the schematic of the model potential used in this paper. Since our main interest in the present paper is the nanoscale structures observed in STM images, we neglect atomic-scale structures and assume constant values V_L and 0 for the potentials in the surface and vacuum regions, respectively. The abrupt change in the potential at the surface-vacuum interface is a good approximation enough to discuss nanometer-scale waves. The screened Coulomb potential given by Eq. (2.2) is added to the constant potentials. The present model is valid only when the depth of the impurity is larger than the screening length.

We simulate the STM image of the subsurface impurities in the GaAs(110) surface where the Friedel oscillation is observed.[9] The Fermi wave number k_F is determined as 0.033 a.u., because the period of the oscillation observed in STM images is about 50 Å, which corresponds to $2\pi/(2k_F)$. The work function W $(=-E_F)$ is chosen as 0.15 a.u., which corresponds to about 4 eV. Therefore, V_L is

determined as $-0.150\,5445$ a.u.

We assume that the screened Coulomb potential is attractive with a $+1$ ionic charge. This is the potential for electrons with an effective mass m^*. To obtain the same wave functions, the potential strength for electrons with a mass m must be multiplied by m^*/m. Therefore, f_0 is determined as $-m^*/m=-0.066$ for the GaAs case. Since $|f_0/k_F|=2$, this is a rather strong scattering. When the range of the potential is extended, the screening effect by the medium is important. This effect is taken into account by dividing the scattering potential by the dielectric constant ϵ. In this case, f_0 is calculated as -0.005, since ϵ of GaAs is 13.13. We perform calculations for both the strong-scattering case with $f_0=-0.066$ and the weak-scattering case with $f_0=-0.005$.

For the screening length $1/\mu$, we choose three values of 30, 10, and 5 Å. The first value is the screening length calculated for InP (Ref. 7) using the scattering theory of bulk impurities.[17] It is reasonable to use the values for InP, because the electronic properties of InP such as the band gap, effective mass, and dielectric constant are similar to those of GaAs. The second value is the surface screening length determined from the interaction between vacancies on the InP(110) surface.[7] The third one is the value of the example shown in the scattering theory of bulk impurities.[17] The first one and the latter two values correspond to the cases of $\mu<k_F$ and $\mu>k_F$, respectively. Therefore, it is expected from the discussion in Sec. II that the Friedel oscillation appears in the latter cases.

Wave functions are solved by the recursion-transfer-matrix (RTM) method.[18] In this method, wave functions are expanded in terms of two-dimensional reciprocal lattice vectors parallel to the surface and are solved by discretizing the one-dimensional differential equation along z axis perpendicular to the surface. Therefore, wave functions of the single-impurity system are obtained by this method using a supercell with a triangular lattice. The lattice constant of the supercell is chosen as 600 a.u., which is 20 times as large as $1/k_F$. The cutoff energy of the reciprocal vectors is 0.005 a.u., which is about 10 times as large as $k_F^2/2$. The interval of meshes discretizing the differential equation along the z axis is 1.25 a.u. which is about 1/24 of $1/k_F$. The differential equation is solved in a region between a plane by 100 a.u. behind the center of the scattering potential and a plane by 20 a.u. above the surface-vacuum interface. The LDOS for obtaining STM images is calculated at a plane by 10 a.u. above the surface-vacuum interface. The results obtained in this section do not change by varying the tip-sample distance, because corrugations of nanoscale lateral waves do not generally depend on the tip-sample distance,[10] as mentioned in Sec. II.

STM images are expressed by a dimensionless function defined as

$$\tilde{\rho}(\tilde{r}_\parallel,\tilde{d})=\ln\left[\frac{\rho(r_\parallel,d)}{\rho(\infty,d)}\right], \tag{3.1}$$

where $\tilde{r}_\parallel\equiv k_F r_\parallel/\pi$ and $\tilde{d}\equiv k_F d$, because the corrugation can be obtained as

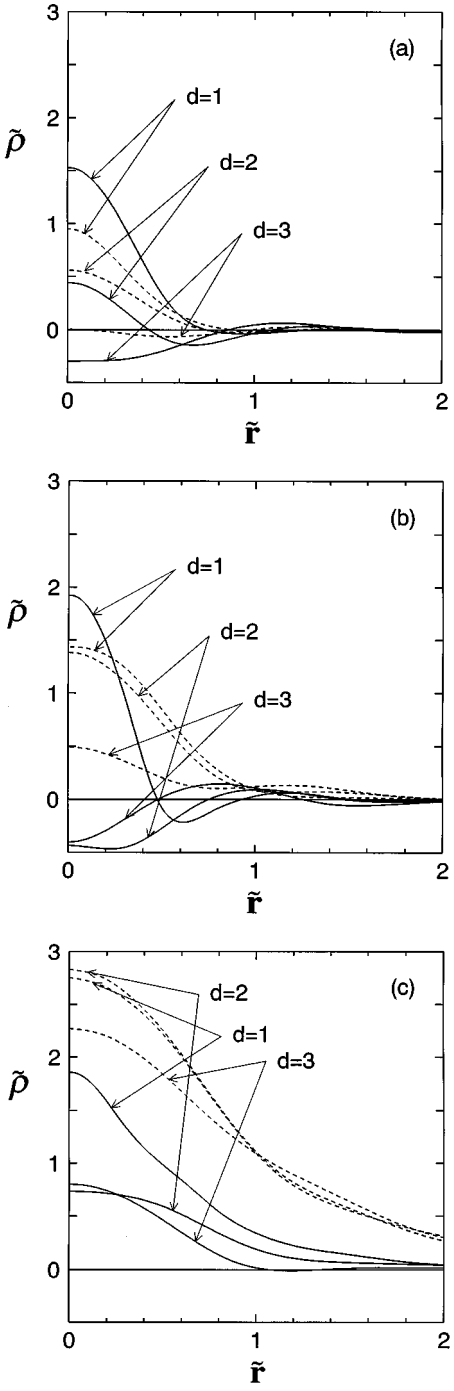

FIG. 2. $\tilde{\rho}$ as a function of $\tilde{r}_\parallel=k_F r_\parallel/\pi$. The screening length $1/\mu$ is (a) 5, (b) 10, and (c) 30 Å. The scattering strength f_0 is -0.066 a.u. Solid lines are exact curves calculated by the RTM method. Dotted lines are perturbative ones calculated using Eq. (2.16). In each figure, three curves are shown for representing the cases that the depth $\tilde{d}$ $(=k_F d)$ of the impurity is 1, 2, and 3.

$$\Delta z=\frac{\tilde{\rho}(\tilde{r}_\parallel,\tilde{d})}{2\sqrt{2W}}. \tag{3.2}$$

Figure 2 shows $\tilde{\rho}$ as a function of $\tilde{r}_\parallel$. The scattering strength f_0 is -0.066, and the screening length $1/\mu$ is (a) 5, (b) 10, and (c) 30 Å. In each figure, three solid curves are

shown for representing the cases of $\tilde{d}=1$, 2, and 3. Curves calculated by the perturbation using Eq. (2.16) are also shown by dotted lines.

As discussed in the previous section, the Friedel oscillation is seen only when $\mu>k_F$ as in Figs. 2(a) and 2(b). When $\mu<k_F$ as in Fig. 2(c), the curves decrease almost monotonously. The dotted lines obtained perturbatively are qualitatively similar to the solid lines calculated exactly, but they differ quantitatively. Especially in the case of Fig. 2(b), the exact curves show the Friedel oscillation, but the perturbative ones do not. This reflects that the present case is a strong scattering, since $|f_0/k_F|=2$. It has been verified that when the scattering strength is as weak as $f_0=-0.005$, the perturbative curves coincide with the exact ones.

The curves also oscillate as a function of the depth of impurities. As the solid curve $\tilde{d}=3$ of Fig. 2(a), there are cases showing negative corrugations at the center of the impurity, in spite of the attractive scattering potential. This means that we cannot determine the sign of the impurity charge simply from the sign of the corrugation.

Typical STM images calculated by the RTM method are shown in Fig. 3. The parameter set of $1/\mu$ and $\tilde{d}$ is chosen as (a) 5 Å and 2, (b) 5 Å and 3, and (c) 30 Å and 2. The scan width in each figure is 2×2 in the unit of π/k_F. The shapes of the images deviate slightly from spherically symmetric, reflecting that the present supercell is not large enough. But, since the deviations are negligible, the present calculations are sufficient. Figure 3(a) shows the Friedel oscillation, but Fig. 3(c) does not, reflecting the difference of the potential ranges. The ring structure shown in Fig. 3(b) is similar to those observed in STM of semiconducting transition-metal-dichalcogenide surfaces.[19–24] They have been interpreted as images of ring-shaped materials buried in the subsurface.[19] In this paper, we interpret them as the Friedel oscillation by subsurface impurities, as discussed in the next section.

Figure 4 shows $\tilde{\rho}$ at $\tilde{r}_\parallel=0$ as a function of the depth $\tilde{d}$ of the impurity. The scattering strength f_0 is -0.066 and the screening length $1/\mu$ is (a) 5 Å and (b) 30 Å. In each figure, closed circles and solid lines show exact values calculated by the RTM method and perturbative ones obtained using Eq. (2.16), respectively. The analytical curves expressed by Eq. (2.27) are shown in Fig. 4(a) by the dotted lines.

In the cases of $\mu>k_F$ as in Fig. 4(a), the curves show the Friedel oscillation. As expected, the exact and perturbative curves differ, because of the strong scattering. It has been verified that they coincide in the weak-scattering case of $f_0=-0.005$. Though they differ quantitatively in the strong-scattering case, qualitative behavior of the corrugation amplitude may generally be summarized as follows. When the depth is smaller than $1/k_F$, the corrugation amplitude increases with the increase of the depth, and reaches the maximum value at the depth of $k_Fd\sim1$. At larger depths, the corrugation decreases as $1/d^2$ with the oscillation of $2k_F$. The analytical curves deviate quantitatively from the perturbative ones at small depths, because the integral part of $q>k_F$ is neglected in deriving Eq. (2.27). But, since the oscillating behavior of the exact curves is well reproduced, they are useful for qualitative discussions.

In the case of $\mu<k_F$ as in Fig. 4(b), the curves do not show the Friedel oscillation, but decrease roughly as a function of the depth d. The oscillating behavior seen slightly in the figure is due to the fact that μ is not much smaller than k_F. In this case also, the perturbative curves deviate considerably from the exact ones owing to the strong scattering.

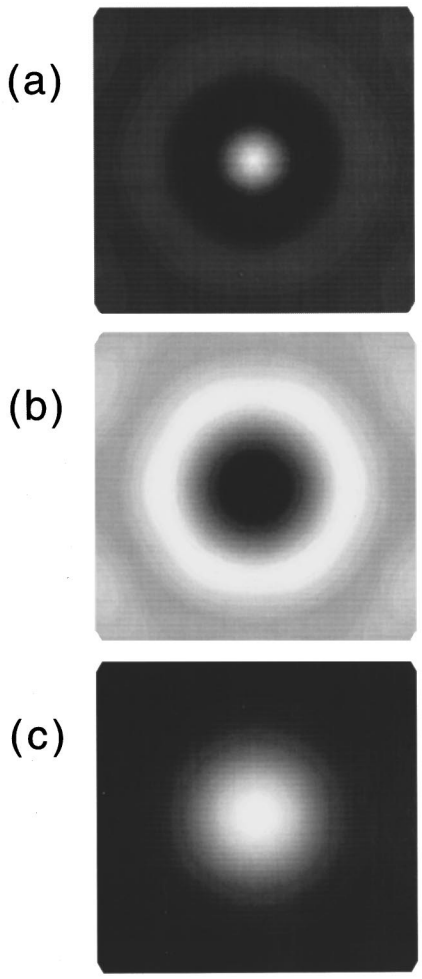

FIG. 3. STM images of the subsurface impurity calculated by the RTM method. The depth $\tilde{d}$ of the impurity is (a),(c) 2 and (b) 3. The screening length $1/\mu$ is (a),(b) 5 and (c) 30 Å. The scattering strength f_0 is -0.066 a.u. The scan width in each figure is 2×2 in the unit of π/k_F.

So far we have presented calculated results for the attractive scattering potential. Figure 5 shows curves for repulsive cases calculated exactly by the RTM method. f_0 is $+0.066$. $1/\mu$ is (a) 5 Å and (b) 30 Å. For comparison, the curves calculated for the attractive potential with $f_0=-0.066$ are shown by dotted lines. Values displayed for the attractive cases are multiplied by -1. The repulsive curves deviate from the attractive ones because the present case with $|f_0|=0.066$ is the strong scattering. When the scattering strength is as weak as $|f_0|=0.005$, we found that the attractive and repulsive curves coincide with a reverse sign. Though profiles of the attractive and repulsive curves are quantitatively different in the strong-scattering cases, it may be concluded generally that the corrugation of a charged impurity is qualitatively reverse to that of an impurity with the opposite sign of charge.

In the case of $\mu<k_F$ as shown in Fig. 5(b), the attractive and repulsive scattering potentials produce the positive and

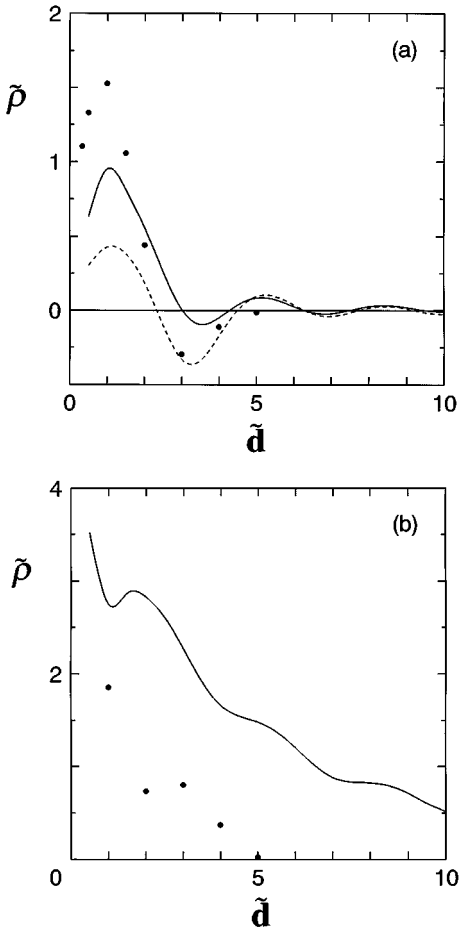

FIG. 4. $\tilde{\rho}$ at $r_{\parallel}=0$ as a function of $\tilde{d}=k_F d$. The scattering strength f_0 is -0.066, and the screening length $1/\mu$ is (a) 5 and (b) 30 Å. Closed circles show exact values calculated by the RTM method. Solid lines are perturbative curves calculated using Eq. (2.16). Dotted lines are approximate ones calculated using the analytical expression shown in Eq. (2.27).

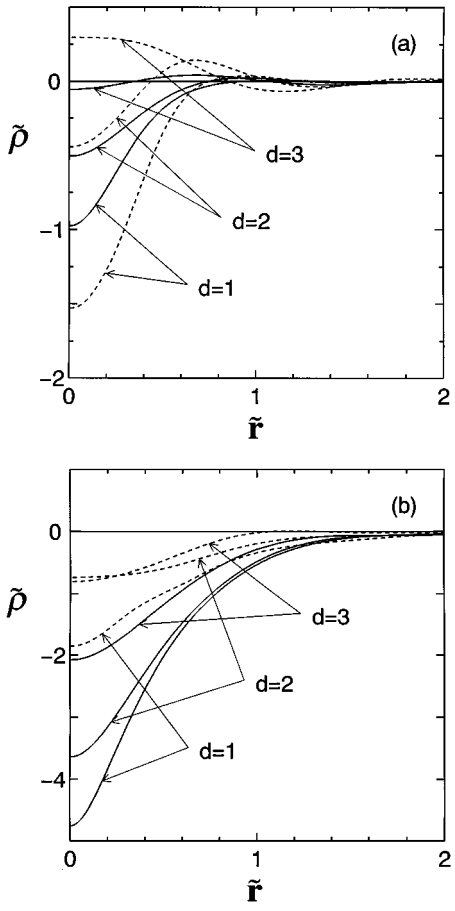

FIG. 5. $\tilde{\rho}$ as a function of $\tilde{r}_{\parallel}=k_F r_{\parallel}/\pi$ for the repulsive scattering potential. Solid curves are calculated by the RTM method with the scattering strength of $f_0=+0.066$. The screening length $1/\mu$ is (a) 5 and (b) 30 Å. The depth $\tilde{d}$ of the impurity is 1, 2, and 3. For comparison, the curves calculated for the attractive cases with $f_0=-0.066$ are shown by dotted lines. Values displayed for the attractive curves are multiplied by -1.

negative corrugations, respectively. This by chance agrees with the intuitive picture that we observe positive and negative corrugations in STM images of donor and acceptor impurities, respectively, because electrons accumulate around the attractive potential and are pushed out by the repulsive potential. The same conclusion holds in the case of $\mu > k_F$, when the depth d is smaller than $1/k_F$.

IV. DISCUSSIONS AND CONCLUSIONS

First, we compare the calculated results with the Friedel oscillations observed experimentally in the STM images of the Si donor in the GaAs(110) surface.[9] We have studied behaviors of electrons scattered by subsurface impurities using the screened Coulomb potential. The Friedel oscillation is obtained only when the range of the scattering potential is shorter than the Fermi wavelength. Therefore, the screening length of the Si donor in the GaAs(110) surface should be smaller than $1/k_F=16$ Å.

The profile of the experimental corrugation seen in Fig. 2(b) of Ref. 9 is similar to that of the curve calculated for $\tilde{d}=1$ shown in Fig. 2(b), where $1/\mu$ is 10 Å. The corrugation amplitude at the peak calculated using Eq. (3.2) is 0.93 Å, which agrees well with the experimental one of about 1 Å. This good agreement between the experimental and calculated values suggests that the screening length and the depth of the observed impurity are about 10 and 16 Å, respectively.

The estimated screening length is consistent with the value of 10.5 ± 1.5 Å determined experimentally for the vacancies on the InP surface.[7] Since the screening length is not very large, the screening effect by the medium would not be important. This is consistent with the fact that the experimental corrugation amplitude agrees well with the theoretical one calculated for the strong-scattering case with $f_0=-0.066$ where the dielectric constant is not taken into account.

At the depth of 16 Å, the corrugation amplitude is at the maximum as shown in Fig. 4(a). Since we expect that subsurface impurities are most clearly observed around this depth, it is probable that the impurities observed in the experiment are buried at this depth. The speculation that the subsurface impurity showing the largest corrugation is buried at the depth of about 16 Å is consistent with the experimental

fact that five kinds of corrugations are observed,[4] because the spacing between layers of the GaAs(110) surface is 2.0 Å, and therefore we expect to observe eight kinds of corrugations at best.

It should be noted that it is possible to observe subsurface impurities at depths greater than 16 Å. They can be distinguished from impurities buried at depths smaller than the depth showing the maximum corrugation by measuring the bias dependence of the corrugation amplitude. By increasing the bias voltage, the Fermi wave number increases, and the effective depth $\tilde{d}=k_F d$ also increases. Therefore, if the corrugation amplitude decreases with the increase of the bias voltage, the depth of impurities would be larger than $1/k_F$.

We can estimate the depth of the subsurface impurity also from the bias dependence of the period of the Friedel oscillation. STM images of subsurface impurities show the Friedel oscillation of $2k_F r$, where r is a function of both the lateral distance $r_\parallel$ and the depth d as $r=\sqrt{r_\parallel{}^2+d^2}$. By changing the bias voltage V, the period of the oscillation also changes, because the Fermi wavelength k_F is proportional to $\sqrt{|V|}$. Here, V is measured from the top of the valence band or the bottom of the conduction band, which may be determined by STS. Therefore, we estimate the depth by tracing the point $r_\parallel$ with the change of the bias voltage where $2k_F r$ is constant. The depth of impurities is given by

$$d=\sqrt{\frac{V_1 r_{\parallel 1}^2-V_2 r_{\parallel 2}^2}{V_2-V_1}}, \tag{4.1}$$

where $r_{\parallel 1}$ and $r_{\parallel 2}$ are the equivalent positions corresponding to two different bias voltages V_1 and V_2.

In the case of the Friedel oscillation observed in Fig. 3 of Ref. 9, we plotted $1/r_\parallel^2$ versus bias voltages, where $r_\parallel$ is defined as half the distance between the two minima, and found an almost linear dependence of the plotted values. This means that the depth of the impurity is much smaller than $r_\parallel \sim 20$ Å. Therefore, the depth of the impurity may be smaller than the value of 16 Å estimated above, but it is beyond the ability of the present simple model for the impurity potential to determine more precisely the depth of the impurity. First-principles calculations are necessary.

The calculated STM image shown in Fig 3(b) resembles the ring structures observed in STM of semiconducting transition-metal-dichalcogenides surfaces. The ring structures are observed on natural MoS_2 surfaces[19] and on ion-bombarded WSe_2 surfaces,[20] but not observed on synthesized MoS_2 surfaces.[19] Similar structures are observed on WSe_2 surfaces modified by mechanical indentations or by applying pulse voltages with STM tips.[21,22] The radii of these ring structures are about 15 Å.[19]

The ring structures have been interpreted as images of ring-shaped molecules buried in the subsurface[19] or as topographical protrusions modified by STM tips.[22] In this paper, however, we interpret them as the Friedel oscillation by single subsurface impurities, because the ring structures are not observed in atomic force microscopy.[19] This fact excludes the possibility of the topographical protrusions. Moreover, the radii of the ring structures can be explained as follows, if we assume that the impurity is buried in the second van der Waals gap between the chalcogen-metal-chalcogen sandwiches.

The ring structure shown in Fig. 3(b) is obtained when the impurity is buried at the depth of $k_F d=2$, where d is about 12 Å in the case of the second van der Waals gap of the transition-metal dichalcogenides. Since the peak of the ring structure is seen at $k_F r_\parallel/\pi \sim 0.8$ in the figure, the radius is calculated as about 15 Å, which agrees well with the observed value. Similarly, the hillocks observed on modified WSe_2 surfaces[20–22] are interpreted as images of subsurface impurities buried in the first van der Waals gap at the depth of $k_F d=1$. Furthermore, the nanometer-scale dark spots observed on ion-bombarded MoS_2 surfaces[25] and alkali-adsorbed MoS_2 surfaces[26] may be interpreted as images of subsurface impurities with the negative corrugations.

Subsurface impurities are well observed on semiconductor surfaces but are not observed on metal surfaces. The reason for this fact is that in semiconductors, the Fermi wave number is small and the screening length is not too small. Since the effective depth $\tilde{d}$ is determined by $k_F d$, the corrugation amplitude decreases rapidly with the increase of d in the case of metals with large k_F. In addition, the scattering strength itself is weak in the metal case, because of the short screening length.

The oscillation of the corrugation amplitude depending on the depth of the impurities is due to the standing waves formed near the surface, which is essentially the same as the energy dependence of the images of subsurface Ar bubbles observed in STM of the aluminum surfaces.[27] However, the origin of the oscillations in the profile of STM images is slightly different. In the case of the subsurface single impurities, the Friedel oscillation is formed by the interference of the incident wave and the waves scattered spherically. On the other hand, it would be better to interpret the oscillation observed in the subsurface bubbles as the diffraction of waves by structures with finite lateral sizes, though it may be also a kind of the Friedel oscillation in a wide sense.

In conclusion, we have studied theoretically STM images of subsurface impurities using the screened Coulomb potential. When the screening length is shorter than the Fermi wavelength, we obtained the Friedel oscillation observed in STM, which is produced by the interference of the incident waves and the waves scattered spherically. STM images also oscillate as a function of the depth of the subsurface impurities, because standing waves are formed near the surface. We obtained various kinds of images of the subsurface impurities such as the ring structures and the images with negative corrugations which are observed in STM of semiconducting transition-metal-dichalcogenide surfaces. When the depth is small, the corrugation amplitude increases with the increase of the depth and reaches the maximum at $d \sim 1/k_F$. We speculate that the impurities observed most clearly in STM are buried at this depth.

The oscillating behavior of STM images presented in this paper is due to the fact that waves with nanoscale lateral dimensions are propagating. Atomic-scale lateral waves decay on the atomic scale.[10] By use of the oscillating behaviors of the nanoscale lateral waves, we can obtain information of subsurface structures by STM.

ACKNOWLEDGMENT

This work is partially supported by a Grant-in-Aid from the Ministry of Education, Science and Culture, Japan.

[1] R. M. Feenstra, J. M. Woodall, and G. D. Pettit, Phys. Rev. Lett. **71**, 1176 (1993).
[2] M. B. Johnson, O. Albrektsen, R. M. Feenstra, and H. W. M. Salemink, Appl. Phys. Lett. **63**, 2923 (1993).
[3] M. B. Johnson, H. P. Meier, and H. W. M. Salemink, Appl. Phys. Lett. **63**, 3636 (1993).
[4] J. F. Zheng, X. Liu, N. Newman, E. R. Weber, D. F. Ogletree, and M. Salmeron, Phys. Rev. Lett. **72**, 1490 (1994).
[5] J. F. Zheng, X. Liu, E. R. Weber, D. F. Ogletree, and M. Salmeron, J. Vac. Sci. Technol. B **12**, 2104 (1994).
[6] Ph. Ebert, M. Heinrich, M. Simon, C. Domke, K. Urban, C. K. Shih, M. B. Webb, and M. G. Lagally, Phys. Rev. B **53**, 4580 (1996).
[7] Ph. Ebert, Xun Chen, M. Heinrich, M. Simon, K. Urban, and M. G. Lagally, Phys. Rev. Lett. **76**, 2089 (1996).
[8] K. -J. Chao, A. R. Smith, and C. -K. Shih, Phys. Rev. B **53**, 6935 (1996).
[9] M. C. M. M. van der Wielen, A. J. A. van Roij, and H. van Kempen, Phys. Rev. Lett. **76**, 1075 (1996).
[10] K. Kobayashi, Phys. Rev. B **53**, 11 091 (1996).
[11] J. D. Levine, Phys. Rev. **140**, A586 (1965).
[12] J. W. Gadzuk, Phys. Rev. **154**, 662 (1967).
[13] V. E. Godwin and W. E. Tefft, Surf. Sci. **34**, 108 (1973).
[14] D. B. MacMillen and U. Landman, J. Chem. Phys. **80**, 1691 (1984); Phys. Rev. B **29**, 4524 (1984).
[15] J. Tersoff and D. R. Hamann, Phys. Rev. Lett. **50**, 1998 (1983); Phys. Rev. B **31**, 805 (1985).
[16] C. J. Chen, Phys. Rev. Lett. **65**, 448 (1990).
[17] R. B. Dingle, Philos. Mag. **46**, 831 (1955).
[18] K. Hirose and M. Tsukada, Phys. Rev. Lett. **73**, 150 (1994); Phys. Rev. B **51**, 5278 (1995).
[19] W. M. Heckl, F. Ohnesorge, G. Binnig, M. Specht, and M. Hashmi, J. Vac. Sci. Technol. B **9**, 1072 (1991).
[20] Th. Schimmel, H. Fuchs, R. Sander, and M. Lux-Steiner, Ultramicroscopy **42-44**, 683 (1992).
[21] H. Fuchs, Th. Schimmel, M. Lux-Steiner, and E. Bucher, Ultramicroscopy **42-44**, 1295 (1992).
[22] H. Fuchs, Th. Schimmel, S. Akari, L. M. Eng, M. Anders, M. Lux-Steiner, and K. Dransfeld, in *Nanosources and Manipulation of Atoms Under High Fields and Temperatures: Applications*, edited by V. T. Binh, N. Garcia, and K. Dransfeld (Kluwer Academic, Dordrecht, Netherlands, 1993), pp. 293–309.
[23] S. N. Magonov, H. -J. Cantow, and M. -H. Whangbo, Surf. Sci. **318**, L1175 (1994).
[24] M. -H. Whangbo, J. Ren, S. N. Magonov, H. Bengel, B. A. Parkinson, and A. Suna, Surf. Sci. **326**, 311 (1995).
[25] N. Sengoku and K. Ogawa, Jpn. J. Appl. Phys. **34**, 3363 (1995).
[26] H. Abe, K. Kataoka, K. Ueno, and A. Koma, Jpn. J. Appl. Phys. **34**, 3342 (1995).
[27] M. Schmid, W. Hebenstreit, and P. Varga, Phys. Rev. Lett. **76**, 2298 (1996).